Electrocatalytic Lignin Depolymerization enabled by a Biomass-derived Iron Dual-Atom Catalyst: from Synthesis to an *In-Operando* X-Ray Absorption Spectroscopy Study

Lucie M. Lindenbeck,[a,b,c] Anuja P. Nawadkar,[b] Dirk Lützenkirchen-Hecht,[d] Andreas Drichel,[a] Marcella Frauscher,[e] Björn B. Beele,[a] Piotr Kuśtrowski,[f] Prathamesh Patil,[g,h] Christian M. Pichler,[g,h] Yu Chen,[i] Yi Yu,[i] Christian W. Lehmann,[c] Jiayin Yuan,[b] Bruno V. M. Rodrigues*[a], and Adam Slabon*[a,j]

[a] Chair of Inorganic Chemistry, Faculty of Mathematics and Natural Sciences, University of Wuppertal, Gaußstraße 20, 42119 Wuppertal, Germany

[b] Department of Materials and Environmental Chemistry (MMK), Stockholm University, 10691 Stockholm, Sweden

[c] Max-Planck-Institut für Kohlenforschung, Kaiser-Wilhelm-Platz 1, 45470 Mülheim an der Ruhr, Germany

[d] Department of Physics, Faculty of Mathematics and Natural Sciences, University of Wuppertal, Gaußstraße 20, 42119 Wuppertal, Germany

[e] AC2T research GmbH, Viktor-Kaplan-Straße 2, 2700 Wiener Neustadt, Austria

[f] Faculty of Chemistry, Jagiellonian University, Gronostajowa 2, 30-387 Krakow, Poland

[g] CEST Centre of Electrochemical and Surface Technology, Viktor Kaplan-Straße 2, 2700 Wiener Neustadt, Austria

[h] TU Wien, Institute of Applied Physics, Wiedner Hauptstrasse 8, 1040 Vienna, Austria

[i] School of Physical Science and Technology & Shanghai Key Laboratory of High-Resolution Electron Microscopy, ShanghaiTech University, 393 Middle Huaxia Road, Pudong, Shanghai, 201210, China

[j] Wuppertal Center for Smart Materials & Systems, University of Wuppertal, 42119 Wuppertal, Germany

KEYWORDS. Electrocatalysis, depolymerization, in-operando XAS, atomically dispersed catalyst, structure determination.

ABSTRACT: Transitioning from crude oil to renewable carbon sources is crucial for a circular economy. Lignin, a byproduct of the paper industry, has significant potential as a renewable feedstock, but its efficient depolymerization remains challenging. This study presents an iron dual-atom catalyst (DAC) supported on biochar derived from spent coffee grounds for the selective electrochemical depolymerization of kraft lignin under ambient conditions. The catalyst was synthesized via pyrolysis and characterized using X-ray absorption spectroscopy (XAS), low-energy ion scattering (LEIS), and X-ray photoelectron spectroscopy (XPS). These techniques confirmed the DAC's atomic dispersion and chemical composition. The DAC's *in-operando* stability was confirmed through XAS under varying electrochemical potentials. In a water/sodium carbonate electrolyte, the DAC achieved lignin depolymerization within 20 h. Nuclear magnetic resonance (NMR) and high-resolution mass spectrometry (HRMS) analyses identified aliphatic products such as sodium acetate and formate, alongside phenolic monomers and dimers. This work demonstrates the potential of DACs for the valorization of biomass while establishing a framework for the monitoring of catalyst behavior at an atomic level during electrochemical biomass depolymerization, thus contributing to the development of advanced catalytic processes.

INTRODUCTION

When employing heterogeneous electrocatalysts, it is imperative to consider potential changes in their structure and chemical environment throughout the course of a reaction.[1] For instance, within the context of the electrochemical CO_2 reduction reaction (eCO_2RR), copper remains as the sole catalyst capable of generating multi-carbon products at viable rates. [2–4] Nevertheless, it has been shown that 7 nm copper nanoparticles undergo substantial transformations, resulting in the formation of larger metallic grains during CO_2RR and the oxidation of Cu_2O nanocubes upon exposure to air after electrolysis. [5,6] These observations highlight the urgent need for a comprehensive understanding of catalyst dynamics within the context of reaction conditions. [1]

X-ray absorption spectroscopy (XAS) methods, including X-ray absorption near-edge structure (XANES) and extended X-ray absorption fine structure (EXAFS), are highly effective for investigating the atomic and electronic structure of atomically dispersed catalytic metal sites, such as single-atom catalysts (SACs) and dual-atom catalysts (DACs), or

https://doi.org/10.26434/chemrxiv-2025-jnt4c **ORCID:** https://orcid.org/0000-0002-0130-8029 Content not peer-reviewed by ChemRxiv. **License:** CC BY-NC-ND 4.0

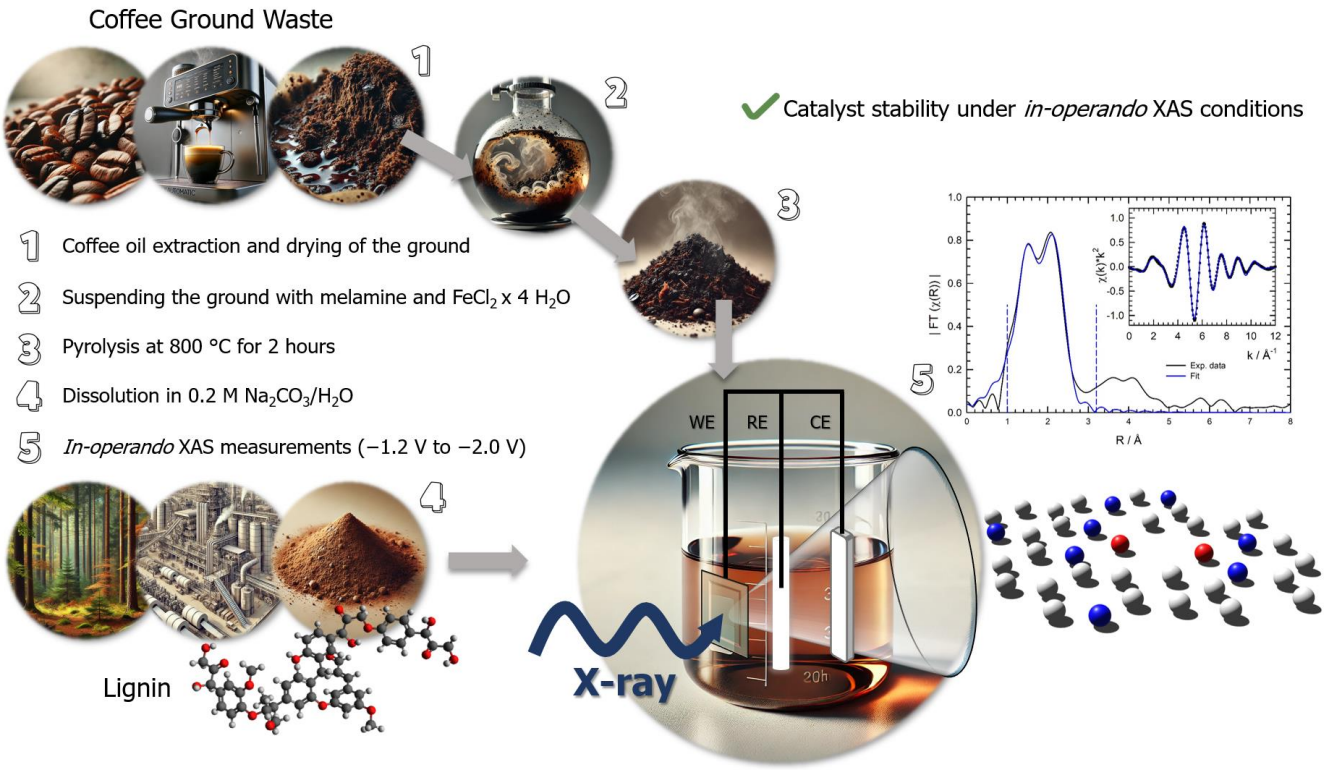

Scheme 1. Schematic representation of the preparation process for the iron DAC, followed by *in-operando* XAS measurements conducted in an aqueous lignin/sodium carbonate medium under varying potentials to evaluate the catalyst's stability

nanoparticles. [7–11] These hard X-ray techniques permit studies to be conducted under conditions that more closely resemble those that would be encountered in a realistic setting; in other words, the catalyst structure can be studied "on duty". [12–14] Improvements in time-resolved XAS have enabled the tracking of reaction dynamics over a timescale that extends from milliseconds to hours. [15–18]

CO_2RR and the electrochemical biomass depolymerization are two processes that share a common objective: addressing global carbon challenges. While CO_2RR directly reduces atmospheric or captured CO_2 by converting it into useful chemicals, biomass depolymerization complements this process by unlocking the potential of renewable carbon stored in complex lignocellulosic polymers. [1] Lignin, a significant component of lignocellulosic biomass and the most substantial natural source of aromatic compounds, is produced on an industrial scale of about 70 million tons [19] as a byproduct of the pulp and paper industry. However, the utilization of lignin for high-value applications remains limited, with only a small percentage (<2%) [20] being employed for such purposes. The majority of lignin is currently incinerated for energy recovery. Lignin's highly crosslinked molecular structure, composed of three primary phenylpropane units by ether and carbon-carbon bonds, along with hydroxyl and methoxy groups, renders it highly resistant to breakdown, [21,22] what makes the selective and efficient depolymerization into high-value added products challenging. [23] This inherent property has hindered its broader utilization. [24] The abundance and inherent aromaticity of lignin, as a feedstock, make it a promising candidate for the sustainable production of value-added chemicals. Lignin depolymerization can be achieved through oxidative and reductive electrochemical approaches. While oxidative methods, which break down lignin via anodic reactions, have been more extensively explored, reductive electrochemical depolymerization remains still heavily unexplored. In a previous study, we demonstrated the first reductive depolymerization of lignin using electrochemical methods under mild conditions. [25]

The majority of studies on electrocatalysts for lignin valorization have focused on bulk electrodes, including carbon, [26–29] nickel, [30–32] platinum, [33] lead, [34–36] and copper. [25] Yet, the structural and chemical diversity of these electrodes is rather limited. [1] So far, studies have focused on bulk, *i.e.* macroscopic, materials whereas nanoscopic or atomically-dispersed catalysts for the reductive depolymerization of lignin, to the best of our knowledge, have not been reported so far. The progress in the eCO_2RR has successfully demonstrated the application of such catalysts to achieve high *Faradaic Efficiencies* (FE) and current densities. Electrocatalytic lignin depolymerization has been so far heavily underresearched within this respect. [37] The progress in catalyst discovery for eCO_2RR and water-splitting using nanostructured materials can be attributed to the increased surface area of nanostructured materials, which provides more active and low-coordinated catalytic sites, and their ability to precisely tailor electronic properties to favor specific reaction pathways. The subsequent evolution from nanoparticular to atomically structured electrodes, such as SACs and DACs, offers promise for further improvement. SACs are composed of discrete metal atoms dispersed across a support material. This configuration enables nearly every metal atom to function as an active site, with the potential to achieve efficiencies as high as 100%. [38] The single-atom

https://doi.org/10.26434/chemrxiv-2025-jnt4c **ORCID:** https://orcid.org/0000-0002-0130-8029 Content not peer-reviewed by ChemRxiv. **License:** CC BY-NC-ND 4.0

configuration permits precise control over the electronic environment surrounding the active sites. SACs can be designed to selectively activate or break specific chemical bonds, thereby enabling high selectivity for targeted reactions. [37] The robust attachment of individual atoms to the support structure confers enhanced stability and mitigates the proclivity for aggregation, thereby outperforming conventional catalysts in these aspects.

Despite the significant strides made in the design of the coordination environment of SACs, they are confronted with a pivotal challenge in the optimization of the adsorption of all reaction intermediates, which is constrained by thermodynamics. [39] This limitation significantly restricts SACs in catalyzing reactions that require the synergistic activation of multiple molecules and intermediates. To address this issue, the concept of DACs has been introduced. The presence of adjacent active sites in DACs offers additional positions for molecule activation and intermediate adsorption, thereby providing an extra level of flexibility for catalytic control. [39]

The terms DAC and SAC may be misleading in that they imply that only the metal atoms have a catalytic effect. Even so, it can be assumed that the matrix also has a catalytic effect. [1] The selection of the matrix is of critical importance to SACs and DACs. Commonly used matrices, such as ZnO, [40] poly(ionic liquid) surface-coated filter paper, [41] bipyridine-based two-dimensional conjugate covalent-organic frameworks, [42] porous nitrogen-substituted carbon, [43] hollow carbon–nitrogen spheres, [44] and nitrogen-substituted carbon nanofibers [45], are predominantly composed of carbon and nitrogen in various commercially available modifications. Since carbon is a major component of biomass, it is logical to use biomass as a carbon source for the matrix. Carbon as a bulk catalyst has already been used for the electrochemical depolymerization of lignin, the substrate of interest in the present study. [26–29] The recent surge in interest surrounding biochar, a material produced through the thermochemical conversion of biomass, can be attributed to its versatility in a multitude of applications. Primarily utilized as a soil amendment, biochar has demonstrated efficacy in reducing greenhouse gas emissions and enhancing soil quality. [46] Additionally, biochar is being employed as a precursor in the synthesis of catalysts and adsorbents for contaminant removal, underscoring its growing utility in various fields. [46] Yet, the use of biomass also presents logistical challenges, such as the need for large-scale harvesting and transportation, which often rely on non-renewable energy sources. These challenges can be mitigated by using biomass waste, as is the case with lignin, which does not require any additional logistical changes as the existing infrastructure can efficiently accommodate its use. [47]

Coffee is among the most extensively traded agricultural commodities globally, with an estimated annual production of approximately 8 billion kilograms. [48] The commercial production of coffee beverages generates vast amounts of spent coffee grounds, which require effective waste management. These byproducts present a significant challenge due to their high oxygen demand during decomposition and the potential release of environmental pollutants, including residual caffeine, tannins, and polyphenols. [49] Nonetheless, novel strategies for the valorization of spent coffee grounds present a sustainable alternative. [48,50,51]

SACs have demonstrated remarkable advancement as efficient catalysts, exhibiting distinctive reactivity and selectivity for biomass conversion. Most studies, though, have concentrated on the conversion of biomass-derived downstream components, including sugars, platform molecules, and small molecules. [37] In contrast, the application of DACs in biomass conversion remains largely unexplored. While bulk electrodes composed e.g. of carbon, [28,29] copper, [25] silver, [52] and nickel [31,32,53] have gained recognition for their application in electrochemical lignin depolymerization, to the best of our knowledge, iron has not yet been utilized in this context. Iron-based DACs have been predominantly studied for other reactions, such as the oxygen reduction reaction [54,55] (ORR), oxygen evolution reaction (OER), [56] and CO_2RR [57]. However, most of these DACs consist of mixed dual atoms, such as iron-nickel [54,57] or iron-cobalt [56,58,59] combinations, rather than purely iron-based systems. This highlights both a significant gap in current research and the as yet untapped potential of DACs, particularly iron-only DACs, for the electrochemical depolymerization of lignin.

In this study, we disclose an iron dual-atom catalyst on coffee waste biochar as electrocatalyst for the reductive depolymerization of kraft lignin towards organic chemicals, both aliphatics and phenolics. This represents a significant advance in the development of atomically structured catalysts, marking a departure from the use of bulk catalysts, such as copper, [25] silver, [52] and carbon, [28,29] which have been the focus of our previous investigations. In this study, our objective is twofold: first, to characterize the catalyst and test its performance and stability under *in-operando* conditions, and second, to examine the electrochemical depolymerization of lignin (**Scheme 1**).

MATERIALS AND METHODS

Materials. The coffee grounds were collected by a fully automated machine with a ceramic grinder and subsequently kept at −18 °C until required for use. Kraft lignin obtained from industrial pulping spent liquor was used as starting material for the lignin depolymerization. All other chemicals were purchased from commercial suppliers and employed in their original, unpurified state. All aqueous solutions were prepared with ultrapure water, obtained from a Millipore system.

Preparation of coffee grounds. The ground coffee waste (30 g) was subjected to three cycles of washing with ultrapure water and subsequent drying at 105 °C for 48 h. The coffee was mixed with n-hexane (50 mL) and heated overnight at 80 °C under reflux. The coffee was separated from the n-hexane by filtration, after which the coffee powder was washed with water and ethanol and dried for 48 h at 105 °C. The n-hexane was removed from the filtrate under reduced pressure, resulting in the isolation of coffee oil with a yield of 8.3% (based on the total weight of the coffee).

Catalyst Preparation. First, 2.0 g of coffee ground waste, 0.5 g of melamine, and 150 mg of $FeCl_2 \times 4\ H_2O$ powder were combined in 30 mL of ethanol and stirred for 1 h, followed by 10 min of sonication in an ultrasonic bath. The ethanol was subsequently removed under reduced pressure, and

https://doi.org/10.26434/chemrxiv-2025-jnt4c **ORCID:** https://orcid.org/0000-0002-0130-8029 Content not peer-reviewed by ChemRxiv. **License:** CC BY-NC-ND 4.0

the residue mixture was subjected to drying at 60 °C over night. Subsequently, the catalyst was synthesized by pyrolyzing the as-prepared material at 800 °C with a heating rate of 5 °C·min^{-1} under a nitrogen atmosphere for 2 h. Subsequently, the furnace was permitted to cool to room temperature. The catalyst was then ground with concentrated hydrochloric acid to remove any excess metallic species. The catalyst was separated from the hydrochloric acid by vacuum filtration and subsequently washed to a pH of 7 with ultrapure water. Finally, the catalyst was washed three times with ethanol and dried overnight at 60 °C. The synthesis process of the control sample (BC) was similar to that of the catalyst, with the exception of the addition of $FeCl_2$ x 4 H_2O during the process.

Electrode Preparation. The electrodes were prepared by first combining 100 mg of the catalyst with 0.8 mL of Nafion™ solution, following by the addition of 0.6 mL of ethanol and 0.6 mL of ultrapure water. Subsequently, the suspension was subjected to ultrasonication for 5 min. Carbon paper (2 cm x 5 cm) was coated with a catalyst suspension (~5 mg·cm^{-1}) on both sides and dried overnight at 60 °C.

Electrochemical Depolymerization of Kraft Lignin. In a standard experiment, kraft lignin was initially dissolved at a concentration of 3 g·L^{-1} in 5 mL of a 2 M aqueous sodium carbonate solution. Subsequently, 45 mL of water was added to this mixture. The electrochemical depolymerization process was conducted with a three-electrode system: a working electrode (carbon paper (CP), biochar coated on carbon paper (BC), dual-atom catalyst coated on carbon paper (DAC)), a platinum mesh counter electrode, and an Ag/AgCl (saturated KCl) reference electrode. Chronoamperometry was performed with a constant potential of −1.6 V. All experiments were conducted at room temperature and ambient pressure. After each reaction, water was removed under reduced pressure, and the resulting solid was dried under the same conditions. The dried solid was then suspended in ethanol and stirred vigorously for 1 h. The remaining residue was filtered off, and ethanol was evaporated from the filtrate under reduced pressure, yielding a white solid.

Nuclear Magnetic Resonance Spectroscopy. Nuclear magnetic resonance (NMR) measurements were performed on a BRUKER Avance 400 MHz spectrometer and on a BRUKER Avance III 600 MHz spectrometer. The following probe heads were used: 5 mm broadband inverse probe with automatic frequency determination, 5 mm QNP probe, and 5 mm broadband inverse probe. Chemical shifts were referenced with respect to Me_4Si.

Direct infusion (DI) ESI-HRMS. Depolymerized lignin samples were dissolved in methanol, ultrasonicated for 30 min and centrifuged for 10 min (14000 rmp). High-resolution mass spectrometry (HRMS) was used as an advanced analytical method to gain the structure information of degradation products of lignin. MS and MSn spectra were obtained using an Orbitrap-IQX high-resolution mass spectrometer (ThermoFisher Scientific, Bremen, Germany), equipped with an ESI source. ESI-MS analyses were carried out in ESI(-) and ESI(+)mode. The solutions were infused into the ESI source via direct infusion (DI) at a rate of 5 µL min^{-1}. Typical spray and ion optics for negative mode conditions were the following: source voltage, 3.0 kV; sheath gas flow rate, 8 arb; capillary temperature, 275 °C; capillary voltage, −50 V; tube lens voltage, −130 V. Fragmentation and interpretation was done based on negative ionization mode, positive ionization mode was used for additional confirmation. Xcalibur version 2.0.7 and Mass Frontier version 8.0 (ThermoFisher Scientific, Bremen, Germany) software were used for data processing and evaluation.

Differential scanning calorimetry and thermogravimetric analysis (DSC/TGA). Differential scanning calorimetry (DSC) and thermogravimetric analysis (TGA) data were obtained using a Netzsch STA 449 F5 Jupiter instrument. Samples were placed in 40 µL Al_2O_3 crucibles closed with Al_2O_3 lids and heated from 20 °C to 800 °C (5 °C·min^{-1}), followed by a period of two hours during which the sample was maintained at 800 °C, under a nitrogen flow (25 mL·min^{-1}).

X−Ray Spectroscopy (XAS). Extended X−ray absorption fine structure (EXAFS) experiments were carried out at the materials science beamline 10 at the DELTA storage ring (TU Dortmund / Germany) operating with 1.5 GeV electrons and a stored current of 100−130 mA[60] (Range: 4−14 keV). A Si (111) channel−cut monochromator was employed, and the intensity of the incident beam on the sample was measured using a nitrogen−gas filled ionization chamber, while the X−ray fluorescence from the sample was collected using a large−area PIPS® photodiode (Passivated Implanted Planar Silicon). The energy range measured covered the X−ray absorption edge of Fe (7112 eV). Fluorescence mode EXAFS data were collected on the fly in the quick−scanning EXAFS mode, in which the Bragg−angle of the monochromator was continuously decreased while each data point in the spectrum is collected within a small integration time of typically 50−100 ms. [61]

X−Ray Spectroscopy Sample Preparation. A small reactor was built for *in-operando* synchrotron radiation measurements. With the catalyst (DAC) coated carbon paper was attached to the front with epoxy resin. Kapton® tape was used to seal the front and back, creating a compartment for the electrolyte. The counter and reference electrodes were fixed in separate chambers.

Low-energy ion scattering spectroscopy (LEIS). Low-energy ion scattering spectroscopy was performed using an ION-TOF Qtac100 spectrometer (IonTOF, Germany). The residual pressure of the LEIS chamber is maintained at 10^{-8} mbar. LEIS experiments were performed using He^+ ions with an energy of 3 keV as the primary beam at an incident angle of 0° and a scattering angle of 145°. The measurement area was 2 mm x 2 mm. A beam of 2 keV Ar^+ ions at an incident angle of 59° was used as sputter cleaning beam to clean the sample from residual contaminations The flux of primary He^+ ions was maintained approximately $1{\cdot}10^{14}$ ion s^{-1}. The total measurement time was $1.1{\cdot}10^4$ s. The time-of-flight (ToF) filter was switched on while measuring the scattered ions. This filters out low-energy ions, which contributes to reducing the background. The charge compensation was switched to minimize charging of the electrically insulating catalyst samples.

The samples were prepared by pressing onto a copper tape with a spatula until firm and then introduced into the chamber.

https://doi.org/10.26434/chemrxiv-2025-jnt4c **ORCID:** https://orcid.org/0000-0002-0130-8029 Content not peer-reviewed by ChemRxiv. **License:** CC BY-NC-ND 4.0

X-ray powder diffraction (XRD). XRD experiments were carried out employing the Bragg-Brentano parafocusing geometry on an X'Pert Pro multi-purpose diffractometer (PanAnalytical, Almelo, The Netherlands). Non-monochromatized Cu Kα radiation (40 kV, 40 mA) was used for irradiation of the powder samples on a rotating zero-background holder, and the scattered intensities were collected with a multi-strip X'celerator detector in an angular range from 2Θ=10 to 110°. The incident beam path was comprised of a vertical divergence slit with an opening angle of 0.5°, a 0.04 rad Soller slit and a fixed horizontal mask (10 mm), respectively. In the diffracted beam path, a 0.02 mm Ni Kβ-filter, a 0.02 Soller slit and an anti-scatter slit were installed.

X-ray photoelectron spectroscopy (XPS). XPS spectra were collected in a Prevac photoelectron spectrometer equipped with a hemispherical analyzer (VG SCIENTA R3000) using monochromatized aluminum Al Kα radiation (E = 1486.6 eV). The binding energy scale was calibrated to the position of XPS C 1s peak at 285.0 eV attributed to adventitious carbon. The data were processed in the Casa XPS software.

Scanning Electron Microscopy with Energy Dispersive X-ray Spectroscopy (SEM-EDX). Energy-dispersive X-ray (EDX) spectroscopy was employed to analyze the catalyst, utilizing a Hitachi TM3030 PLUS tabletop scanning electron microscope with an Oxford EDX detector.

Inductively coupled plasma optical emission spectrometry (ICP-OES). The samples were digested in an HNO_3/HCl mixture (1 mL ddH_2O, 250 µL HNO_3, 250 µL HCl) and the iron content was measured using inductively coupled plasma-optical emission spectrometry (ICP-OES; Avio 220 Max, PerkinElmer).

High-resolution transmission electron microscopy (HR-TEM). HR-TEM images were performed on a JEOL JEM-F200 microscope (Cs: ~1 mm), operated at 200 kV with a field-emission gun and a Gatan Rio16 camera.

RESULTS AND DISCUSSION

We employed a supported iron dual-atom catalyst (DAC) synthesized from coffee waste biochar for the reductive electrochemical depolymerization of kraft lignin. For the preparation of the catalyst matrix, the coffee oil has been removed from the coffee grounds using n-hexane. This approach presents two major advantages. First, the coffee oil does not interfere with the pyrolysis process, where it could otherwise vaporize and subsequently condense in the furnace. Second, the coffee oil can be reused, aligning with the principles of *Green Chemistry* by converting a waste product into a valuable resource. For instance, it could serve as a *green* lubricant. [50] It should be noted that the focus of this study was not on characterizing the oil. The relevant data can be found in the Supporting Information, which includes ^{1}H, ^{13}C, ^{1}H ^{1}H-COSY, and ^{1}H ^{13}C-HSQC NMR (**Figure S1-4**).

To simulate and gain a deeper understanding of the pyrolysis conditions within the furnace, the mixture of coffee residues, melamine, and iron chloride, which had not yet undergone carbonization, was subjected to a thermogravimetric analysis (TGA) (Error! Reference source not found.). At the onset of the heating process, up to 254 °C, the TGA curve exhibits a minimal loss of mass (~ −6%), predominantly attributable to the evaporation of residual moisture and the initial evaporation of highly volatile organic constituents within the coffee ground and melamine. In the primary decomposition phase, between 254 °C and 600 °C, there is a pronounced reduction in mass as organic compounds are thermally decomposed, yielding smaller, volatile molecules. These processes contribute to the formation of a carbon-rich structure in the sample. Upon reaching 800 °C, the sample was maintained at this temperature for 2 h to facilitate the formation of a stable, carbon-rich structure. At this stage, the TGA curve exhibits only minimal additional mass loss, indicating that most of the volatile components have already been released. Carbonization at even higher temperature was not tested as the previous study indicated an iron-catalyzed graphitization step occurring rapidly above 850 °C. [62]

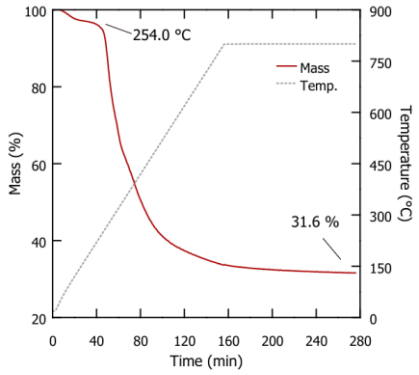

Figure 1. Thermogravimetric analysis (TGA) for the mixture of coffee ground, melamine, and iron chloride. The sample was heated from 20 °C to 800 °C, at a rate of 5 °C·min^{-1}. Next, the sample was maintained at 800 °C for 2 h under a nitrogen flow (25 mL·min^{-1}), which was sufficient to simulate the pyrolysis process occurring within the furnace.

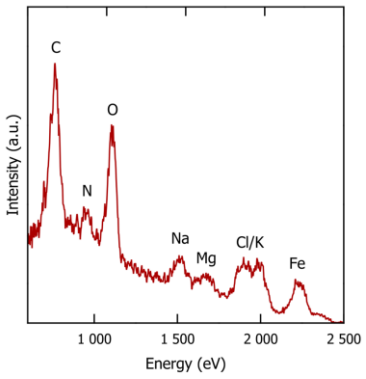

Figure 2. Low-energy ion scattering (LEIS) spectrum of DAC. The spectrum provides confirmation of the surface composition of the DAC, exhibiting peaks for carbon, nitrogen, and oxygen derived from the biochar matrix and melamine, in addition to iron peaks, which are indicative of successful doping. Furthermore, trace elements such as magnesium, sodium, potassium, and chlorine are detected, originating from the coffee precursor and $FeCl_2$.

https://doi.org/10.26434/chemrxiv-2025-jnt4c **ORCID:** https://orcid.org/0000-0002-0130-8029 Content not peer-reviewed by ChemRxiv. **License:** CC BY-NC-ND 4.0

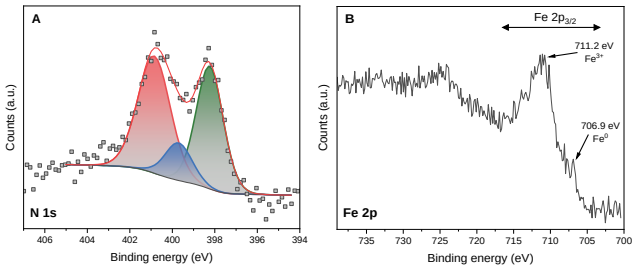

Figure 3. XPS N 1s (A) and Fe 2p (B) core level spectra of DAC. The XPS N 1s spectrum reveals peaks attributed to pyridinic (green), pyrrolic (blue), and quaternary (red) nitrogen species, indicating successful nitrogen doping of the biochar matrix. Furthermore, the Fe 2p spectrum validates the presence of Fe^{3+} as the predominant oxidation state, accompanied by a negligible contribution from metallic Fe.

The final mass stabilized at approximately 31.6 %, reflecting the catalyst yield after pyrolysis and confirming the efficacy of the pyrolysis conditions in producing the desired product.

Low-energy ion scattering spectroscopy (LEIS) measurements were performed on the DAC (**Figure 2**). Coffee is known to contain major amounts of caffeine, but it is also rich in numerous phytochemicals, including phenols (such as chlorogenic acid and caffeic acid), diterpenes (such as cafestol and kahweol), lactones, niacin, and trigonelline, which is the precursor of niacin. [63–65] In total, there are almost 1000 defined phytochemicals in coffee. [66] The peaks observed in the LEIS spectrum can be attributed to the presence of carbon, nitrogen, and oxygen, which can be explained by the addition of melamine and the above-mentioned components of coffee. The successful doping of the coffee by the iron species is corroborated by the presence of a peak that can be assigned to iron. Furthermore, magnesium, sodium, potassium and chloride have been identified as minor constituents of coffee. [63,67,68] It is plausible that the chloride present is augmented by the introduction of $FeCl_2$.

Similarly to the LEIS measurement, a SEM-EDX measurement (**Figure S5**) enabled the detection of carbon, nitrogen, oxygen, iron, sodium, potassium, and chlorine. Furthermore, the sample exhibited the presence of calcium, magnesium, aluminum, phosphorus, and sulfur, which are also known components of coffee. [67,69]

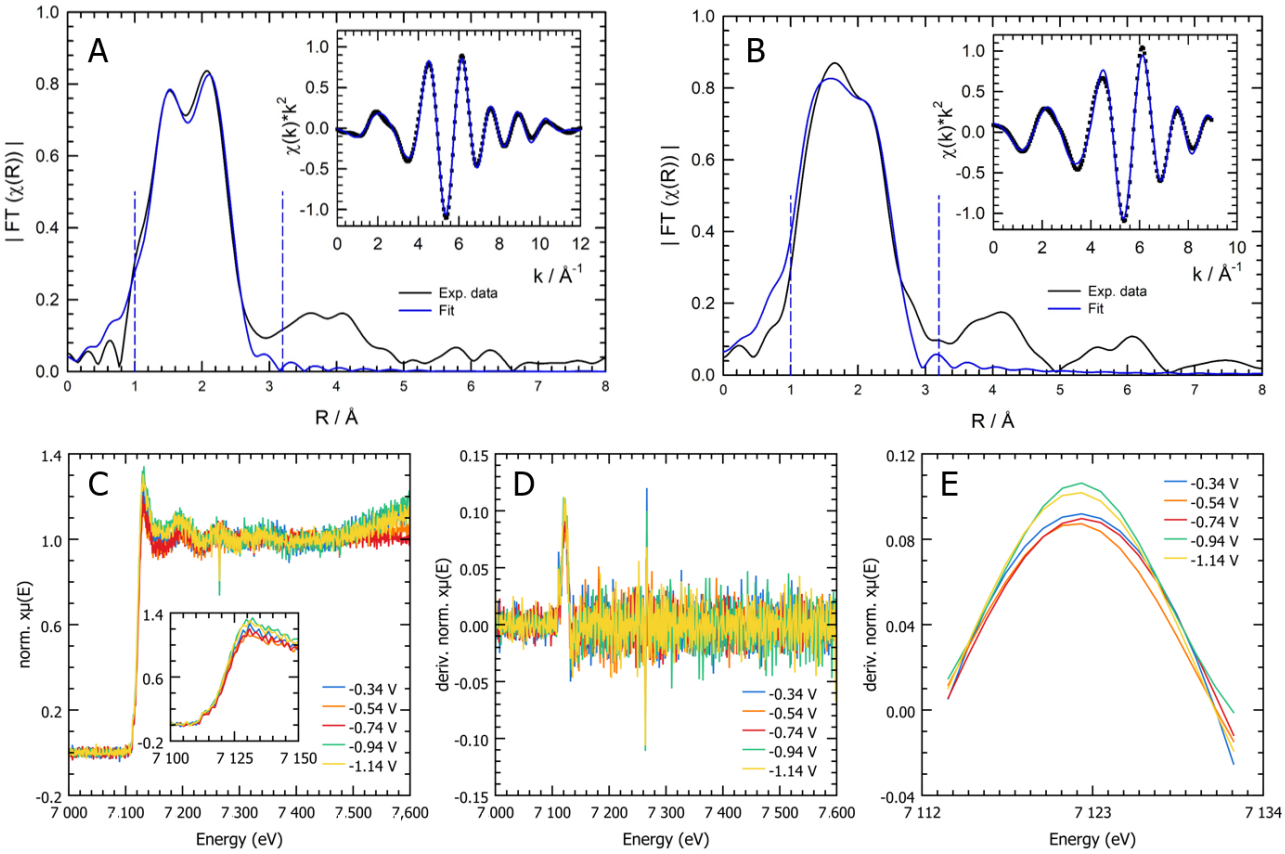

Figure 4. Coordination structure and stability of DAC. **A** Fourier transform (FT) of the Fe K-edge EXAFS spectrum of DAC pre-reaction and corresponding fitting curve (k-range for the FT 1.3 $Å^{-1}$ < k < 11.6 $Å^{-1}$). The inset depicts the back-transformed data from 1.0 Å < R < 3.2 Å according to the dashed vertical lines. **B** Fourier transformation of the Fe K-edge EXAFS spectrum of DAC post-reaction and corresponding fitting curve, again the range from 1.0 Å < R < 3.2 Å was back-transformed into k-space and is depicted in the inset. **C** Normalized Fe K-edge XAS spectra measured *in-operando* for different potentials (*vs.* RHE) as indicated. **D** First derivation of the normalized Fe K-edge XAS spectra. **E** Gaussian fit for the first derivative in the edge region (7112 eV < E < 7143 eV) of the normalized Fe K-edge XAS spectra. No systematic shift of the edge positive is observed.

https://doi.org/10.26434/chemrxiv-2025-jnt4c **ORCID:** https://orcid.org/0000-0002-0130-8029 Content not peer-reviewed by ChemRxiv. **License:** CC BY-NC-ND 4.0

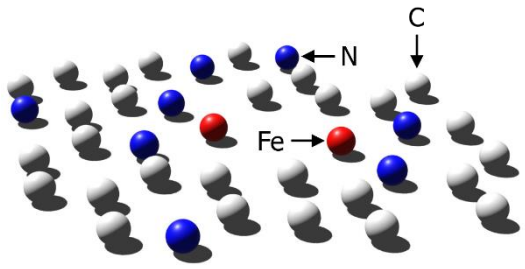

Figure 5. Structural model, based on fitting results, for DAC comprising a N_2-Fe-Fe-N_2 motif. The model illustrates the coordination environment of the dual-atom active sites in the DAC. Fitting results from XAS and extended EXAFS analysis confirm the presence of Fe-N and Fe-Fe bonds, along with carbon interactions from the biochar matrix.

The iron content of the DAC was determined to be 2.81 % by inductively coupled plasma optical emission spectrometry (ICP-OES). Additionally, the iron content of a biochar (BC) sample, which did not undergo the $FeCl_2$ addition, was also quantified as a reference. A negligible quantity of iron (0.01 %) was identified in this sample, as iron is a known component of coffee. [67]

The picture of the surface composition given by LEIS was supplemented by X-ray photoelectron spectroscopy (XPS), another technique well-suited for surface analysis, but also providing additional information about the chemical state of elements. In addition to carbon and oxygen, which are the main components of the surface of DAC, the presence of significant amounts of N was identified. The XPS N 1s spectrum (**Figure 3A**) shows three components at 398.3 eV, 399.7 eV, and 400.9 eV assigned to pyridinic, pyrrolic, and quaternary nitrogen species, respectively. [70,71] In the case of the component at 399.7 eV, the contribution of Fe-N_x bonds resulting from the interaction between the d-orbitals of Fe and p-orbitals of N cannot be excluded. [72]

Conversely, the analysis of the XPS Fe 2p spectrum (**Figure 3B**) discloses that Fe^{3+} is a dominant iron-containing form on the studied surface. Its presence is confirmed by the position and multiplet structure of the main peak at 710.6 eV in the Fe $2p_{3/2}$ region. [73] Still, a very weak peak at 706.9 eV is observed on the shoulder on the side of lower binding energies, indicating the occurrence of traces of strongly reduced species, most probably metallic Fe.

High-resolution transmission electron microscopy (HR-TEM) was utilized to examine the structure of the catalyst. As documented in literature, atomically dispersed metal atoms, particularly those supported on carbon materials, are potentially vulnerable to high-energy electron irradiation, which can result in the structural collapse of the support and the aggregation of originally dispersed metal atoms during TEM analysis. [74] In a similar manner, in this study, the coffee waste biochar and iron atoms exhibited sensitivity to electron irradiation, complicating the analysis and leading to iron aggregation. A representative image is provided in the Supporting Information (**Figure S6**).

In order to achieve a more profound comprehension of the structure of DAC, X-ray powder diffraction experiments (**Figure S7**) were conducted on DAC and BC as a reference. The XRD patterns of DAC and BC, both exhibit two prominent broad reflection peaks at 23° and 43°, corresponding to the (002) and (101) reflections of the graphitic phase, respectively. [41] Furthermore, the presence of a weak reflection peak around 80°, attributed to the (112) reflection, suggests the occurrence of long-range graphitic stacking, thereby indicating that DAC and BC can be classified as turbostratic carbons. [41]

To gain insight into the coordination structure of the iron atoms in DAC, X-ray absorption (XAS) measurements, that may provide a detailed picture of the atomic environment around the metal centers [75,76] were conducted. The Fourier-transformed (FT) X-ray absorption fine structure (EXAFS) spectrum of DAC (**Figure 4A**) exhibits two peaks at about 1.5 Å and 2.1 Å, indicative of the presence of a Fe-N (1.98 ± 0.03 Å) and a Fe-Fe (2.58 ± 0.03 Å) bond. Furthermore, also carbon from the matrix is detectable in a distance of 2.66 ± 0.05 Å. Most important, compared to metallic Fe in a body-centered cubic structure with 8 iron neighbors in the first shell, the magnitude of the peak at 2.1 Å belonging to Fe-Fe interactions in the first shell is a factor of about ≈ 5 smaller (see **Figure S8**), a strong indication for a substantially reduced Fe-Fe coordination number. Accordingly, a Fe-Fe coordination number of about 1.6 can already be anticipated for sample DAC from the inspection of the Fourier-transformed data, which is confirmed by the quantitative fits (**Figure 4A**). Second, the second Fe-Fe shell, expected at a radial distance of about 2.9 Å, is absent in the raw data. If such a shell is included in the fit model, the resulting amplitude is zero, i.e., there are no small iron clusters in the sample, which would also reveal Fe second nearest neighbor atoms. The fitting results (**Figure 4A**) thus suggested a structural model for DAC comprising a N_2-Fe-Fe-N_2 motif (**Figure 5**). Assuming that iron and nitrogen are incorporated in graphene sheets of the carbon matrix, a simple 2-dimensional model appears sufficient here. To ascertain the stability of the catalyst, the measurement was repeated post-reaction (after lignin depolymerization: −1.6 V (*vs.* Ag/AgCl (satd. KCl) for 20 h). The same structural motif (N_2-Fe-Fe-N_2) was observed to fit (**Figure 4B**) after the reaction, with identical Fe-N and Fe-Fe bond distances of and only slightly changed coordination numbers, indicating that the catalyst remains stable throughout the course of the reaction.

For stability assessment of the catalyst, *in-operando* XAS measurements were conducted, contingent on the potential. To this end, a reactor was designed in which the electrochemical lignin depolymerization could be conducted concurrently with the XAS measurement. The theoretical (**Figure S10**) and practical (**Figure S11**) configuration of the reactor is detailed in the Supporting Information. Due to the high absorbance of the lignin solution, only fluorescence XAS-data could be detected. **Figure 4C** depicts the normalized Fe K-edge XAS spectra at applied potentials of −1.2, −1.4, −1.6, −1.8, and −2.0 V (*vs.* Ag/AgCl (satd. KCl)) (−0.34, −0.54, −0.74, −0.94, and −1.14 V (*vs.* RHE)), respectively. Although the *in-operando* data is noisier than the *ex-situ* measurements due to the significantly lower fluorescence intensity under *in-operando* conditions, all spectra exhibit identical edge positions as well as post-edge absorption minima and maxima. This indicates that the catalyst does not undergo substantial alterations as a function of potential. To verify this assertion with greater precision, the absorption

https://doi.org/10.26434/chemrxiv-2025-jnt4c **ORCID:** https://orcid.org/0000-0002-0130-8029 Content not peer-reviewed by ChemRxiv. **License:** CC BY-NC-ND 4.0

edge was observed and examined for energy shifts, that would be a sensitive indicator, e.g., for potential-induced changes of the Fe-valence. **Figure 4D** depicts the first derivative of the spectra. Due to the inherent noise in the spectra, a Gaussian fit was performed for the first derivative of the absorption edge (**Figure 4E**). No discernible shifts are evident, confirming that the catalyst maintains stability across a range of potentials.

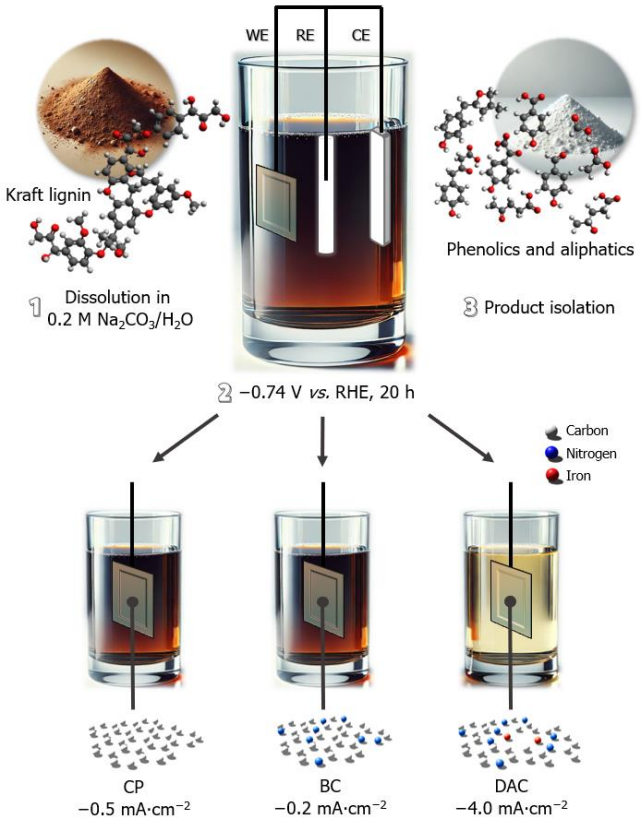

Figure 6. Representation of electrocatalytic depolymerization and partial dearomatization of kraft lignin (3 g·L^{-1}) in an aqueous sodium carbonate medium catalyzed by carbon paper (CP), biochar without Fe-doping (BC) or DAC. The process involves the application of a constant potential (−0.74 V *vs.* RHE), driving the electrochemical reduction of lignin. The selective cleavage of lignin results in the formation of both aliphatic compounds (e.g., sodium levulinate, sodium 4-hydroxyvalerate sodium formate, sodium hexanoate, and sodium acetate) and aromatic species, which are selectively extracted using ethanol as a solvent.

Although DACs have demonstrated efficacy in other catalytic processes due to their synergistic active sites, their potential in addressing the structural complexity of biomass, such as lignin and cellulose, has yet to be fully realized. To address this gap, the performance the DAC was evaluated using the reductive depolymerization of kraft lignin as a representative reaction. This model reaction was selected to substantiate the catalytic activity and stability of the DAC under realistic electrochemical conditions. The principal aim of this study was not to optimize the depolymerization process but to demonstrate the DAC's capacity to facilitate biomass valorization while maintaining structural integrity.

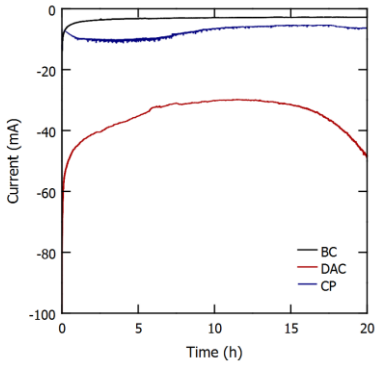

Figure 7. Constant potential electrocatalytic depolymerization at −0.74 V *vs.* RHE of Kraft lignin in 0.2 M Na_2CO_3/H_2O. The DAC demonstrates the highest and most stable current throughout the reaction, reaching −48.4 mA (−4.0 mA·cm^{-2}) by the reaction's completion, thereby exhibiting a significant performance level that surpasses that of CP and BC. The CP electrode displays a consistent but low current of −6.4 mA (−0.5 mA·cm^{-2}), while BC exhibits minimal catalytic activity with a current of −2.8 mA (−0.2 mA·cm^{-2}).

The DAC was successful in enabling lignin depolymerization, resulting in the production of both aliphatic and phenolic compounds. Qualitative observations, such as the decolorization of the lignin solution, provided visual evidence of the reaction's progress (**Figure 6, Figure S12**). The selection −1.6 V as the potential (*vs.* Ag/AgCl (satd. KCl)) (−0.74 V *vs.* RHE) was based on the premise of maintaining a potential below that required for water splitting (E > 1.23 V *vs.* RHE) [77] throughout the reaction, irrespective of pH fluctuations.

Figure 7 illustrates the current course during the 20-hour reaction for DAC and CP and BC for comparison. The DAC exhibits the highest and most sustained current, reaching −48.4 mA (−4.0 mA·cm^{-2}) at the completion of the reaction, which is significantly higher than that observed for the other materials.

In contrast, the CP and BC electrodes demonstrate much lower currents, with CP maintaining a consistent but weak performance (−6.4 mA, −0.5 mA·cm^{-2}) and BC exhibiting minimal activity throughout the reaction (−2.8 mA, −0.2 mA·cm^{-2}). These results underscore the superior catalytic activity of the DAC.

Following the depolymerization reaction, the lignin products (**DL**) were extracted via solid–liquid extraction using ethanol as the solvent. The selection of ethanol was based on its incompatibility with the electrolyte, sodium carbonate, which ensures minimal interaction and a cleaner product separation. Furthermore, ethanol's reusability and status as a safe, sustainable solvent, endorsed by CHEM21, make it an ideal choice for this process. [52]

Table 1 presents a list of the phenolic monomers and dimers that can be identified in DL through DI ESI-HRMS analysis. **Table 2** illustrates the relative intensity of the resulting phenolic products as a function of the employed electrocatalyst, demonstrating the impact of catalyst selection on the observed product distribution.

https://doi.org/10.26434/chemrxiv-2025-jnt4c **ORCID:** https://orcid.org/0000-0002-0130-8029 Content not peer-reviewed by ChemRxiv. **License:** CC BY-NC-ND 4.0

Table 1.Identified phenolic products of depolymerization identified by direct infusion (DI) ESI-HRMS.

m/z	121.0292	137.0272	149.0605	151.0400	165.0193
	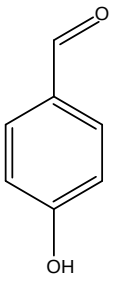	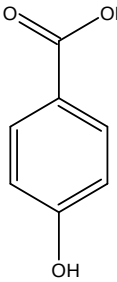	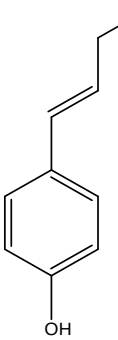	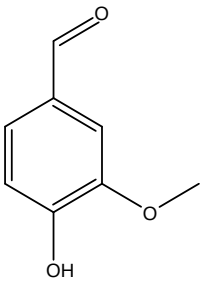	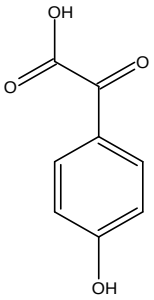
Name	4-hydroxybenzal-dehyde	4-hydroxyben-zoic acid	(E)-4-(3-hydroxyprop-1-en-1-yl)phenol	4-hydroxy-3 methox-ybenzaldehyde	2-(4-hydroxyphenyl)-2 oxoacetic acid
m/z	165.0552	189.0915	193.0504	195.0297	195.0661
	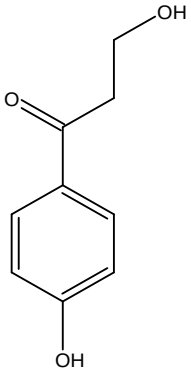	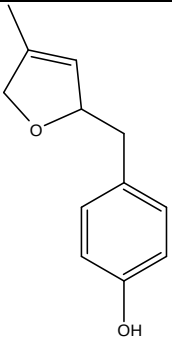	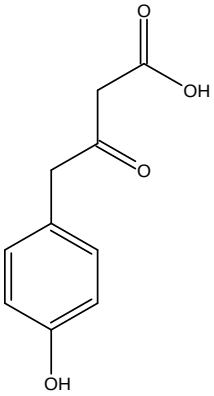	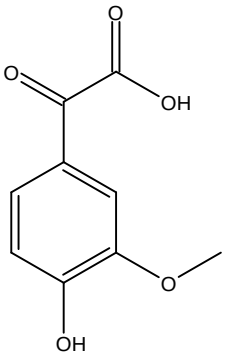	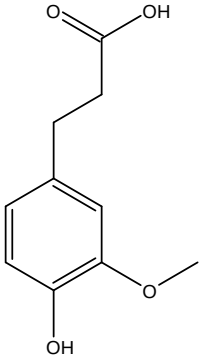
Name	3-hydroxy-1-(4-hydroxy-phenyl)propan-1-one	4-((4-methyl-2,5-dihydrofu-ran-2-yl)me-thyl)phenol	4-(4-hydroxyphenyl)-3-oxobutanoic acid	2-(4-hydroxy-3-methox-yphenyl)-2-oxoacetic acid	3-(4-hydroxy-3 methox-yphenyl)propanoic acid

Table 2. Relative intensity of the phenolic products in the depolymerization products as a function of the electrocatalyst.

m/z	CP	BC	DAC
121.0292			
137.0272			
149.0605			
151.0400			
165.0193			
165.0552			
189.0915			
193.0504			
195.0297			
195.0661			
Intensity	maximum	medium	low

The DI ESI-HRMS analysis revealed the presence of aliphatic compounds, including the products known for lignin depolymerization, [28,29] levulinic acid (115.0400 m/z) and 4-hydroxyvaleric acid (117.0556 m/z), in low intensity. Additionally, hexanoic acid (115.0763 m/z) was identified. Furthermore, formic acid and acetic acid, which are also known aliphatic products of lignin depolymerization, [28,29,52] were detected with the help of a nuclear magnetic resonance (NMR) analysis.

Further analyses and discussions are presented in the Supporting Information (SI).

CONCLUSION

This study introduces an iron dual-atom catalyst (DAC) supported on biochar derived from spent coffee grounds for the electrochemical reductive depolymerization and partial dearomatization of Kraft lignin. The DAC's atomically dispersed iron sites exhibited high catalytic efficiency and selectivity under ambient conditions. *In-operando* XAS confirmed the catalyst's structural stability across varying electrochemical potentials, thereby ensuring consistent performance throughout the reaction. Building on the

https://doi.org/10.26434/chemrxiv-2025-jnt4c **ORCID:** https://orcid.org/0000-0002-0130-8029 Content not peer-reviewed by ChemRxiv. **License:** CC BY-NC-ND 4.0

demonstrated stability and effective depolymerization of lignin into aliphatic and phenolic products, this study highlights the potential of the DAC for innovative biomass valorization. By integrating innovative catalyst design with *in-operando* characterization, a framework for the broader application of dual-atom catalysts is established, and a model for exploring structure-performance relationships in electrochemical systems is provided. These findings pave the way for new opportunities in the rational design and optimization of catalysts tailored to efficient and scalable biomass conversion processes.

AUTHOR INFORMATION

Corresponding Author

* Bruno V. M. Rodrigues - Chair of Inorganic Chemistry; E-mail manzolli@uni-wuppertal.de

*Adam Slabon - Chair of Inorganic Chemistry; E-mail slabon@uni-wuppertal.de

ACKNOWLEDGMENT

We would like to thank the University of Wuppertal and the Stockholm University for their research support. Parts of the results presented here have been achieved through collaborative research projects made possible by the financial support of our project partners and the Austrian COMET program (Project InTribology2, No. 906860). The COMET program is funded by the Austrian federal government and, specifically for InTribology, by the provinces of Lower Austria and Vorarlberg. The XPS study was carried out using research infrastructure funded by the European Union in the framework of the Smart Growth Operational Programme, Measure 4.2; Grant No. POIR.04.02.00-00-D001/20, "ATOMIN 2.0 – Center for materials research on ATOMic scale for the INnovative economy". The financial support of the Strategic Programme Excellence Initiative at Jagiellonian University, used for servicing measurement systems, is also appreciated. We thank the Gesellschaft für Forschungsförderung Niederösterreich (Project FTI21-D002) and the European Regional Development Fund under grant number WST3-F-542638/004-2021 for financial support. A.N. and J.Y. thank the Swedish Research Council for Sustainable Development (FORMAS) for financial support. We thank Andjelka Ristic for her significant contribution to the DI-ESI-HRMS measurement and Julia Bornhorst and Vivien Michaelis for their support with the ICP-OES measurement. In addition, we are grateful for the beam time provided by the DELTA synchrotron (Dortmund, Germany). We would also like to express our appreciation to Madlin Spiewak for her support with the XAS measurements and Franka Stallmann for her support throughout the whole project. We thank Dr. Serhiy Budnyk for the fruitful discussions. L. M. L. appreciates the support and enriching interdisciplinary discussions provided by the Sustainable Chemical Synthesis 2.0 (*SusChemSys 2.0*) networking program.

REFERENCES

(1) Lindenbeck, L. M.; Beele, B. B.; Lützenkirchen-Hecht, D. F.; Rodrigues, B. V. M.; Slabon, A. Electrochemical Biomass Depolymerization: Will Complex Catalysts Trigger High Product Selectivity? *Chem. Mater.* **2024**, *36* (19), 9173–9188. https://doi.org/10.1021/acs.chemmater.4c02078.

(2) Zhu, J.; Mulder, T.; Rokicińska, A.; Lindenbeck, L. M.; Van Den Hoek, J.; Havenith, R. W. A.; V. Cunha, A.; Kuśtrowski, P.; Slabon, A.; Das, S.; Cool, P. Synergistic Interaction between the Ni-Center and Glycine-Derived N-Doped Porous Carbon Material Boosts Electrochemical CO_2 Reduction. *ACS Catal.* **2024**, 10987–10997. https://doi.org/10.1021/acscatal.4c00881.

(3) Phan, H.; Gueret, R.; Martínez-Pardo, P.; Valiente, A.; Jaworski, A.; Slabon, A.; Martín-Matute, B. Synthesis of Benzoic Acids from Electrochemically Reduced CO_2 Using Heterogeneous Catalysts. *ChemSusChem* **2024**, e202401084. https://doi.org/10.1002/cssc.202401084.

(4) Woldu, A. R.; Huang, Z.; Zhao, P.; Hu, L.; Astruc, D. Electrochemical CO2 Reduction (CO2RR) to Multi-Carbon Products over Copper-Based Catalysts. *Coord. Chem. Rev.* **2022**, *454*, 214340. https://doi.org/10.1016/j.ccr.2021.214340.

(5) Kim, D.; Kley, C. S.; Li, Y.; Yang, P. Copper Nanoparticle Ensembles for Selective Electroreduction of CO_2 to C_2–C_3 Products. *Proc. Natl. Acad. Sci. U.S.A.* **2017**, *114* (40), 10560–10565. https://doi.org/10.1073/pnas.1711493114.

(6) Feijóo, J.; Yang, Y.; Fonseca Guzman, M. V.; Vargas, A.; Chen, C.; Pollock, C. J.; Yang, P. *Operando* High-Energy-Resolution X-Ray Spectroscopy of Evolving Cu Nanoparticle Electrocatalysts for CO_2 Reduction. *J. Am. Chem. Soc.* **2023**, *145* (37), 20208–20213. https://doi.org/10.1021/jacs.3c08182.

(7) *X-Ray Absorption: Principles, Applications, Techniques of EXAFS, SEXAFS and XANES*; Koningsberger, D. C., Ed.; Chemical analysis; Wiley: New York, 1988.

(8) Yuan, K.; Lu, C.; Sfaelou, S.; Liao, X.; Zhuang, X.; Chen, Y.; Scherf, U.; Feng, X. In Situ Nanoarchitecturing and Active-Site Engineering toward Highly Efficient Carbonaceous Electrocatalysts. *Nano Energy* **2019**, *59*, 207–215. https://doi.org/10.1016/j.nanoen.2019.02.043.

(9) Yuan, K.; Lützenkirchen-Hecht, D.; Li, L.; Shuai, L.; Li, Y.; Cao, R.; Qiu, M.; Zhuang, X.; Leung, M. K. H.; Chen, Y.; Scherf, U. Boosting Oxygen Reduction of Single Iron Active Sites via Geometric and Electronic Engineering: Nitrogen and Phosphorus Dual Coordination. *J. Am. Chem. Soc.* **2020**, *142* (5), 2404–2412. https://doi.org/10.1021/jacs.9b11852.

(10) Xue, J.; Dong, X.; Liu, C.; Li, J.; Dai, Y.; Xue, W.; Luo, L.; Ji, Y.; Zhang, X.; Li, X.; Jiang, Q.; Zheng, T.; Xiao, J.; Xia, C. Turning Copper into an Efficient and Stable CO Evolution Catalyst beyond Noble Metals. *Nat. Commun.* **2024**, *15* (1), 5998. https://doi.org/10.1038/s41467-024-50436-4.

(11) Meng, L.; Kao, C.-W.; Wang, Z.; Ma, J.; Huang, P.; Zhao, N.; Zheng, X.; Peng, M.; Lu, Y.-R.; Tan, Y. Alloying and Confinement Effects on Hierarchically Nanoporous CuAu for Efficient Electrocatalytic Semi-Hydrogenation of Terminal Alkynes. *Nat. Commun.* **2024**, *15* (1), 5999. https://doi.org/10.1038/s41467-024-50499-3.

(12) Timoshenko, J.; Roldan Cuenya, B. *In Situ* / *Operando* Electrocatalyst Characterization by X-Ray Absorption Spectroscopy. *Chem. Rev.* **2021**, *121* (2), 882–961. https://doi.org/10.1021/acs.chemrev.0c00396.

(13) Fabbri, E.; Abbott, D. F.; Nachtegaal, M.; Schmidt, T. J. Operando X-Ray Absorption Spectroscopy: A Powerful Tool toward Water Splitting Catalyst Development. *Curr. Opin. Electrochem.* **2017**, *5* (1), 20–26. https://doi.org/10.1016/j.coelec.2017.08.009.

(14) Fang, L.; Seifert, S.; Winans, R. E.; Li, T. Operando XAS/SAXS: Guiding Design of Single-Atom and Subnanocluster Catalysts. *Small Methods* **2021**, *5* (5), 2001194. https://doi.org/10.1002/smtd.202001194.

(15) Müller, O.; Nachtegaal, M.; Just, J.; Lützenkirchen-Hecht, D.; Frahm, R. Quick-EXAFS Setup at the SuperXAS Beamline for *in Situ* X-Ray Absorption Spectroscopy with 10 Ms Time Resolution. *J. Synchrotron Radiat.* **2016**, *23* (1), 260–266. https://doi.org/10.1107/S1600577515018007.

(16) Bornmann, B.; Kläs, J.; Müller, O.; Lützenkirchen-Hecht, D.; Frahm, R. The Quick EXAFS Setup at Beamline P64 at PETRA III for up to 200 Spectra per Second; Taipei, Taiwan, 2019; p 040008. https://doi.org/10.1063/1.5084609.

(17) Briois, V.; La Fontaine, C.; Belin, S.; Barthe, L.; Moreno, T.; Pinty, V.; Carcy, A.; Girardot, R.; Fonda, E. ROCK: The New Quick-

https://doi.org/10.26434/chemrxiv-2025-jnt4c **ORCID:** https://orcid.org/0000-0002-0130-8029 Content not peer-reviewed by ChemRxiv. **License:** CC BY-NC-ND 4.0

EXAFS Beamline at SOLEIL. *J. Phys.: Conf. Ser.* **2016**, *712*, 012149. https://doi.org/10.1088/1742-6596/712/1/012149.

(18) Lin, S.-C.; Chang, C.-C.; Chiu, S.-Y.; Pai, H.-T.; Liao, T.-Y.; Hsu, C.-S.; Chiang, W.-H.; Tsai, M.-K.; Chen, H. M. Operando Time-Resolved X-Ray Absorption Spectroscopy Reveals the Chemical Nature Enabling Highly Selective CO2 Reduction. *Nat Commun* **2020**, *11* (1), 3525. https://doi.org/10.1038/s41467-020-17231-3.

(19) Berlin, A.; Balakshin, M. Industrial Lignins. In *Bioenergy Research: Advances and Applications*; Elsevier, 2014; pp 315–336. https://doi.org/10.1016/B978-0-444-59561-4.00018-8.

(20) Davis, K.; Rover, M.; Brown, R.; Bai, X.; Wen, Z.; Jarboe, L. Recovery and Utilization of Lignin Monomers as Part of the Biorefinery Approach. *Energies* **2016**, *9* (10), 808. https://doi.org/10.3390/en9100808.

(21) Li, C.; Zhao, X.; Wang, A.; Huber, G. W.; Zhang, T. Catalytic Transformation of Lignin for the Production of Chemicals and Fuels. *Chem. Rev.* **2015**, *115* (21), 11559–11624. https://doi.org/10.1021/acs.chemrev.5b00155.

(22) Stöcker, M. Biofuels and Biomass-To-Liquid Fuels in the Biorefinery: Catalytic Conversion of Lignocellulosic Biomass Using Porous Materials. *Angew. Chem. Int. Ed.* **2008**, *47* (48), 9200–9211. https://doi.org/10.1002/anie.200801476.

(23) Sun, Z.; Fridrich, B.; De Santi, A.; Elangovan, S.; Barta, K. Bright Side of Lignin Depolymerization: Toward New Platform Chemicals. *Chem. Rev.* **2018**, *118* (2), 614–678. https://doi.org/10.1021/acs.chemrev.7b00588.

(24) Slabon, A.; Rodrigues, B. V. M. To Break, or Not to Break: Is Selective Depolymerization of Lignin a Riemann Hypothesis Rather than a Solution? *Green Chem.* **2024**, 10.1039.D4GC05439C. https://doi.org/10.1039/D4GC05439C.

(25) Da Cruz, M. G. A.; Gueret, R.; Chen, J.; Piątek, J.; Beele, B.; Sipponen, M. H.; Frauscher, M.; Budnyk, S.; Rodrigues, B. V. M.; Slabon, A. Electrochemical Depolymerization of Lignin in a Biomass-based Solvent. *ChemSusChem* **2022**, *15* (15), e202201246. https://doi.org/10.1002/cssc.202201246.

(26) Oh, H.; Choi, Y.; Shin, C.; Nguyen, T. V. T.; Han, Y.; Kim, H.; Kim, Y. H.; Lee, J.-W.; Jang, J.-W.; Ryu, J. Phosphomolybdic Acid as a Catalyst for Oxidative Valorization of Biomass and Its Application as an Alternative Electron Source. *ACS Catal.* **2020**, *10* (3), 2060–2068. https://doi.org/10.1021/acscatal.9b04099.

(27) Fang, Z.; Jackson, J. E.; Hegg, E. L. Mild, Electroreductive Lignin Cleavage: Optimizing the Depolymerization of Authentic Lignins. *ACS Sustainable Chem. Eng.* **2022**, *10* (23), 7545–7552. https://doi.org/10.1021/acssuschemeng.2c00820.

(28) Lindenbeck, L. M.; Barra, V. C.; Dahlhaus, S.; Brand, S.; Wende, L.; Beele, B. B.; Schebb, Nils. H.; Rodrigues, B. V. M.; Slabon, A. Organic Chemicals from Wood: Selective Depolymerization and Dearomatization of Lignin via Aqueous Electrocatalysis. *ChemSusChem* **2024**, e202301617. https://doi.org/10.1002/cssc.202301617.

(29) Lindenbeck, L. M.; Dahlhaus, S.; Wende, L. M.; Beele, B. B.; Frauscher, M.; Schebb, N. H.; Lehmann, C. W.; Bornhorst, J.; Slabon, A.; Rodrigues, B. V. M. Breaking down Lignin in Gamma-Valerolactone: Advances into a Bioelectrorefinery. *Green Chem. Lett. Rev.* **2024**, *17* (1), 2390867. https://doi.org/10.1080/17518253.2024.2390867.

(30) Klein, J.; Waldvogel, S. R. Selective Electrochemical Degradation of Lignosulfonate to Bio-Based Aldehydes. *ChemSusChem* **2023**, *16* (8), e202202300. https://doi.org/10.1002/cssc.202202300.

(31) Carkner, A.; Tageldin, I.; Han, J.; Seifitokaldani, A.; Kopyscinski, J. Impact of Temperature an Order of Magnitude Larger Than Electrical Potential in Lignin Electrolysis with Nickel. *ChemSusChem* **2023**, e202300795. https://doi.org/10.1002/cssc.202300795.

(32) Di Fidio, N.; Timmermans, J. W.; Antonetti, C.; Raspolli Galletti, A. M.; Gosselink, R. J. A.; Bisselink, R. J. M.; Slaghek, T. M. Electro-Oxidative Depolymerisation of Technical Lignin in Water Using Platinum, Nickel Oxide Hydroxide and Graphite Electrodes. *New J. Chem.* **2021**, *45* (21), 9647–9657. https://doi.org/10.1039/D1NJ01037A.

(33) Hasan, M.; Akbari, A.; Greenlee, L. F. Combined Electrocatalytic Oxidation and Reduction to Selectively Cleave β-O-4 Linkage of Lignin over Platinum Electrode in Organic Solvent: Secondary Treatment Opportunity for CELF Process. *ACS Sustainable Chem. Eng.* **2023**, *11* (42), 15262–15272. https://doi.org/10.1021/acssuschemeng.3c03191.

(34) Wang, Y.; Yang, F.; Liu, Z.; Yuan, L.; Li, G. Electrocatalytic Degradation of Aspen Lignin over Pb/PbO2 Electrode in Alkali Solution. *Catal. Commun.* **2015**, *67*, 49–53. https://doi.org/10.1016/j.catcom.2015.03.033.

(35) Liu, M.; Wen, Y.; Qi, J.; Zhang, S.; Li, G. Fine Chemicals Prepared by Bamboo Lignin Degradation through Electrocatalytic Redox between Cu Cathode and Pb/PbO $_2$ Anode in Alkali Solution. *ChemistrySelect* **2017**, *2* (17), 4956–4962. https://doi.org/10.1002/slct.201700881.

(36) Wu, Z.; Zhang, X.; Fan, H.; Han, X.; Wen, Y.; Li, G.; Li, H. Allyl Halide Induced Electrochemical Degradation of Lignin into Double-Bonded Phenolic Monomers. *Int. J. Biol. Macromol.* **2023**, *242*, 124947. https://doi.org/10.1016/j.ijbiomac.2023.124947.

(37) Chen, J.-Y.; Xiao, Y.; Guo, F.-S.; Li, K.-M.; Huang, Y.-B.; Lu, Q. Single-Atom Metal Catalysts for Catalytic Chemical Conversion of Biomass to Chemicals and Fuels. *ACS Catal.* **2024**, *14* (7), 5198–5226. https://doi.org/10.1021/acscatal.4c00208.

(38) Wang, W.; Li, S.; Qiang, Q.; Wu, K.; Pan, X.; Su, W.; Cai, J.; Shen, Z.; Yang, Y.; Li, C.; Zhang, T. Catalytic Refining Lignin-Derived Monomers: Seesaw Effect between Nanoparticle and Single-Atom Pt. *Angew. Chem. Int. Ed.* **2024**, e202404683. https://doi.org/10.1002/anie.202404683.

(39) Zhao, S.; Liu, M.; Qu, Z.; Yan, Y.; Zhang, Z.; Yang, J.; He, S.; Xu, Z.; Zhu, Y.; Luo, L.; Hui, K. N.; Liu, M.; Zeng, J. Cascade Synthesis of Fe-N_2-Fe Dual-Atom Catalysts for Superior Oxygen Catalysis. *Angew. Chem. Int. Ed.* **2024**, e202408914. https://doi.org/10.1002/anie.202408914.

(40) Zhang, H.; Guo, G.; Wang, Z.; He, X.; Ji, H. The Impact of Milling Energy on the Structure of Catalysts during the Mechanochemical Synthesis of Single-Atom Catalysts. *Ind. Eng. Chem. Res.* **2024**, *63* (45), 19530–19536. https://doi.org/10.1021/acs.iecr.4c03272.

(41) Wang, Y.; Wan, L.; Cui, P.; Tong, L.; Ke, Y.; Sheng, T.; Zhang, M.; Sun, S.; Liang, H.; Wang, Y.; Zaghib, K.; Wang, H.; Zhou, Z.; Yuan, J. Porous Carbon Membrane-Supported Atomically Dispersed Pyrrole-Type FeN_4 as Active Sites for Electrochemical Hydrazine Oxidation Reaction. *Small* **2020**, *16* (31), 2002203. https://doi.org/10.1002/smll.202002203.

(42) Dai, L.; Lv, J.; Xu, S.; Zong, J.; Liang, L.; Wang, B.; Li, P. Construction of Interlayered Single-Atom Active Sites on Bipyridine-Based 2D Conjugated Covalent-Organic Frameworks for Boosting the C_2 Products of Electrochemical CO_2 Reduction. *ACS Appl. Mater. Interfaces* **2024**, acsami.4c16371. https://doi.org/10.1021/acsami.4c16371.

(43) Huang, M.; Zhou, S.-H.; Yang, C.-J.; Dong, C.-L.; He, Y.; Wei, W.; Li, X.; Zhu, Q.-L.; Huang, Z. Selenic Acid Etching Assisted Atomic Engineering for Designing Metal-Semimetal Dual Single-Atom Catalysts for Enhanced CO_2 Electroreduction. *ACS Nano* **2024**, acsnano.4c12576. https://doi.org/10.1021/acsnano.4c12576.

(44) Wagh, N. K.; Shinde, S. S.; Lee, J.-H. Atomically Modulated Cu Single-Atom Catalysts for Oxygen Reduction Reactions towards High-Power Density Zn– and Al–Air Batteries. *Chem. Commun.* **2024**, 10.1039.D4CC05217J. https://doi.org/10.1039/D4CC05217J.

(45) Zhao, H.; Song, B.; Li, H.; Li, X.; Ge, C.; Wu, Q.; Chen, J.; Wang, Z.; Yan, G.; Fang, J. Controllable Microwave Heating for Energy-Efficient and Universal Synthesis of Atomically Dispersed Metals on Nitrogen-Doped Carbon Nanofibers. *Small* **2024**, 2407700. https://doi.org/10.1002/smll.202407700.

(46) Qian, K.; Kumar, A.; Zhang, H.; Bellmer, D.; Huhnke, R. Recent Advances in Utilization of Biochar. *Renewable Sustainable*

https://doi.org/10.26434/chemrxiv-2025-jnt4c **ORCID:** https://orcid.org/0000-0002-0130-8029 Content not peer-reviewed by ChemRxiv. **License:** CC BY-NC-ND 4.0

Energy Rev. **2015**, *42*, 1055–1064. https://doi.org/10.1016/j.rser.2014.10.074.

(47) Lindenbeck, L. M.; Barra, V. C.; Beele, B. B.; Rodrigues, B. V. M.; Slabon, A. Revisiting the Electrocatalyst Role on Lignin Depolymerization. *Adv. Energy Sustainability Res.* **2024**, 2400130. https://doi.org/10.1002/aesr.202400130.

(48) Vardon, D. R.; Moser, B. R.; Zheng, W.; Witkin, K.; Evangelista, R. L.; Strathmann, T. J.; Rajagopalan, K.; Sharma, B. K. Complete Utilization of Spent Coffee Grounds To Produce Biodiesel, Bio-Oil, and Biochar. *ACS Sustainable Chem. Eng.* **2013**, *1* (10), 1286–1294. https://doi.org/10.1021/sc400145w.

(49) Silva, M. A.; Nebra, S. A.; Machado Silva, M. J.; Sanchez, C. G. THE USE OF BIOMASS RESIDUES IN THE BRAZILIAN SOLUBLE COFFEE INDUSTRY. *Biomass Bioenergy* **1998**, *14* (5–6), 457–467. https://doi.org/10.1016/S0961-9534(97)10034-4.

(50) Pichler, J.; Maria Eder, R.; Widder, L.; Varga, M.; Marchetti-Deschmann, M.; Frauscher, M. Moving towards Green Lubrication: Tribological Behavior and Chemical Characterization of Spent Coffee Grounds Oil. *Green Chem. Lett. Rev.* **2023**, *16* (1), 2215243. https://doi.org/10.1080/17518253.2023.2215243.

(51) Yu, M.; Chan, C. K.; Tüysüz, H. Coffee-Waste Templating of Metal Ion-Substituted Cobalt Oxides for the Oxygen Evolution Reaction. *ChemSusChem* **2018**, *11* (3), 605–611. https://doi.org/10.1002/cssc.201701877.

(52) Lindenbeck, L.; Brand, S.; Stallmann, F.; Barra, V.; Frauscher, M.; Beele, B. B.; Slabon, A.; Rodrigues, B. V. M. Silver-Catalyzed Aqueous Electrochemical Valorization of Soda Lignin into Aliphatics and Phenolics. *Polymers* **2024**, *16* (23). https://doi.org/10.3390/polym16233325.

(53) Aguillón-Rodríguez, P.; Pérez-Reyes, O.; Ortiz-Cervantes, C. Hydrogenolysis of Lignin and Lignin-Based Molecules Catalyzed by Nickel and Sc(OTf)3. *Res. Chem.* **2023**, *5*, 100729. https://doi.org/10.1016/j.rechem.2022.100729.

(54) Tamtaji, M.; Li, Y.; Cai, Y.; Liu, H.; Goddard Iii, W. A.; Chen, G. Reaction Mechanism and Kinetics of Oxygen Reduction Reaction on the Iron–Nickel Dual Atom Catalyst. *J. Mater. Chem. A* **2023**, *11* (46), 25410–25421. https://doi.org/10.1039/D3TA05694E.

(55) Li, Q.; Luo, L.; Xu, C.; Song, S.; Wang, Y.; Zhang, L.; Tang, Y.; Texter, J. Palladium Enhanced Iron Active Site – An Efficient Dual-Atom Catalyst for Oxygen Electroreduction. *Small* **2023**, *19* (38), 2303321. https://doi.org/10.1002/smll.202303321.

(56) Bai, L.; Hsu, C.-S.; Alexander, D. T. L.; Chen, H. M.; Hu, X. A Cobalt–Iron Double-Atom Catalyst for the Oxygen Evolution Reaction. *J. Am. Chem. Soc.* **2019**, *141* (36), 14190–14199. https://doi.org/10.1021/jacs.9b05268.

(57) Chen, Y.; Zhao, J.; Pan, X.; Li, L.; Yu, Z.; Wang, X.; Ma, T.; Lin, S.; Lin, J. Tuning the Inter-Metal Interaction between Ni and Fe Atoms in Dual-Atom Catalysts to Boost CO_2 Electroreduction. *Angew. Chem. Int. Ed.* **2024**, *136* (44), e202411543. https://doi.org/10.1002/ange.202411543.

(58) Woo, D.; Kim, J.; Xu, L.; Park, J.; Park, C.; Yi, S. Y.; Kim, S.; Jun, H.; Kim, S.; Lee, J. Selective Self-Assembly of Atomically Dispersed Iron and Cobalt Dual Atom Catalyst on Anisotropic Mesoporous Carbon Particles for High Performance Seawater Batteries. *Adv. Funct. Materials* **2024**, 2414749. https://doi.org/10.1002/adfm.202414749.

(59) Jiang, M.; Wang, F.; Yang, F.; He, H.; Yang, J.; Zhang, W.; Luo, J.; Zhang, J.; Fu, C. Rationalization on High-Loading Iron and Cobalt Dual Metal Single Atoms and Mechanistic Insight into the Oxygen Reduction Reaction. *Nano Energy* **2022**, *93*, 106793. https://doi.org/10.1016/j.nanoen.2021.106793.

(60) Lützenkirchen-Hecht, D.; Wagner, R.; Szillat, S.; Hüsecken, A. K.; Istomin, K.; Pietsch, U.; Frahm, R. The Multi-Purpose Hard X-Ray Beamline BL10 at the DELTA Storage Ring. *J. Synchrotron Radiat.* **2014**, *21* (4), 819–826. https://doi.org/10.1107/S1600577514006705.

(61) Frahm, R. Quick Scanning Exafs: First Experiments. *Nucl. Instrum. Methods Phys. Res., Sect. A* **1988**, *270* (2–3), 578–581. https://doi.org/10.1016/0168-9002(88)90732-2.

(62) Yuan, J.; Giordano, C.; Antonietti, M. Ionic Liquid Monomers and Polymers as Precursors of Highly Conductive, Mesoporous, Graphitic Carbon Nanostructures. *Chem. Mater.* **2010**, *22* (17), 5003–5012. https://doi.org/10.1021/cm1012729.

(63) Baspinar, B.; Eskici, G.; Ozcelik, A. O. How Coffee Affects Metabolic Syndrome and Its Components. *Food Funct.* **2017**, *8* (6), 2089–2101. https://doi.org/10.1039/C7FO00388A.

(64) Alton Spiller, M. The Chemical Components of Coffee. In *Caffeine*; Spiller, G. A., Ed.; CRC Press, 2019; pp 97–161. https://doi.org/10.1201/9780429126789-6.

(65) Gómez-Ruiz, J. Á.; Leake, D. S.; Ames, J. M. In Vitro Antioxidant Activity of Coffee Compounds and Their Metabolites. *J. Agric. Food Chem.* **2007**, *55* (17), 6962–6969. https://doi.org/10.1021/jf0710985.

(66) Cano-Marquina, A.; Tarín, J. J.; Cano, A. The Impact of Coffee on Health. *Maturitas* **2013**, *75* (1), 7–21. https://doi.org/10.1016/j.maturitas.2013.02.002.

(67) Mussatto, S. I.; Machado, E. M. S.; Martins, S.; Teixeira, J. A. Production, Composition, and Application of Coffee and Its Industrial Residues. *Food Bioprocess Technol.* **2011**, *4* (5), 661–672. https://doi.org/10.1007/s11947-011-0565-z.

(68) Alcazar, A. Ion Chromatographic Determination of Some Organic Acids, Chloride and Phosphate in Coffee and Tea. *Talanta* **2003**, *61* (2), 95–101. https://doi.org/10.1016/S0039-9140(03)00244-3.

(69) Fraňková, A.; Drábek, O.; Havlík, J.; Száková, J.; Vaněk, A. The Effect of Beverage Preparation Method on Aluminium Content in Coffee Infusions. *Journal of Inorganic Biochemistry* **2009**, *103* (11), 1480–1485. https://doi.org/10.1016/j.jinorgbio.2009.06.012.

(70) Jaramillo, D.; Alvarez, G.; Díaz, C.; Pérez, S.; Muñoz Saldaña, J.; Sierra, L.; López, B. L.; Moreno-Zuria, A.; Mohamedi, M.; Palacio, R. Porous Carbonaceous Materials Simultaneously Dispersing N, Fe and Co as Bifunctional Catalysts for the ORR and OER: Electrochemical Performance in a Prototype of a Zn–Air Battery. *Dalton Trans.* **2024**, *53* (7), 3143–3158. https://doi.org/10.1039/D3DT03330A.

(71) Szewczyk, I.; Rokicińska, A.; Michalik, M.; Chen, J.; Jaworski, A.; Aleksis, R.; Pell, A. J.; Hedin, N.; Slabon, A.; Kuśtrowski, P. Electrochemical Denitrification and Oxidative Dehydrogenation of Ethylbenzene over N-Doped Mesoporous Carbon: Atomic Level Understanding of Catalytic Activity by^{15} N NMR Spectroscopy. *Chem. Mater.* **2020**, *32* (17), 7263–7273. https://doi.org/10.1021/acs.chemmater.0c01666.

(72) Lei, G.; Lin, X.; Yan, H.; Shen, L.; Wang, S.; Liang, S.; Zhao, Z.-J.; Liu, F.; Zhan, Y.; Jiang, L. Valence Electron and Coordination Structure Guided Metal Active Site Design for Hydrolytic Cleavage of Carbon–Sulfide Double Bonds. *ACS Catal.* **2024**, 17103–17112. https://doi.org/10.1021/acscatal.4c02921.

(73) Benedet, M.; Barreca, D.; Rizzi, G. A.; Maccato, C.; Wree, J.-L.; Devi, A.; Gasparotto, A. Fe2O3-Graphitic Carbon Nitride Nanocomposites Analyzed by XPS. *Surf. Sci. Spectra* **2023**, *30* (2), 024021. https://doi.org/10.1116/6.0002979.

(74) Lang, R.; Du, X.; Huang, Y.; Jiang, X.; Zhang, Q.; Guo, Y.; Liu, K.; Qiao, B.; Wang, A.; Zhang, T. Single-Atom Catalysts Based on the Metal–Oxide Interaction. *Chem. Rev.* **2020**, *120* (21), 11986–12043. https://doi.org/10.1021/acs.chemrev.0c00797.

(75) Sheng, B.; Chu, Y.; Cao, D.; Xia, Y.; Liu, C.; Chen, S.; Song, L. Application of X-Ray Absorption Spectroscopy in Carbon-Supported Electrocatalysts. *Nano Res.* **2023**, *16* (11), 12438–12452. https://doi.org/10.1007/s12274-023-6153-5.

(76) Lützenkirchen-Hecht, D.; Yuan, K.; Eckelt, F.; Braun, F.; Voss, L.; Li, L.; Tang, X.; Zhuang, X.; Chen, Y. Investigation of Single Atom Catalysts by X-Ray Absorption Spectroscopy. *Physica Status Solidi (a)* **2024**, 2400606. https://doi.org/10.1002/pssa.202400606.

(77) Wang, T.; Tao, L.; Zhu, X.; Chen, C.; Chen, W.; Du, S.; Zhou, Y.; Zhou, B.; Wang, D.; Xie, C.; Long, P.; Li, W.; Wang, Y.; Chen, R.; Zou, Y.; Fu, X.-Z.; Li, Y.; Duan, X.; Wang, S. Combined Anodic and

https://doi.org/10.26434/chemrxiv-2025-jnt4c **ORCID:** https://orcid.org/0000-0002-0130-8029 Content not peer-reviewed by ChemRxiv. **License:** CC BY-NC-ND 4.0

Cathodic Hydrogen Production from Aldehyde Oxidation and Hydrogen Evolution Reaction. *Nat. Catal.* **2021**, *5* (1), 66–73. https://doi.org/10.1038/s41929-021-00721-y.

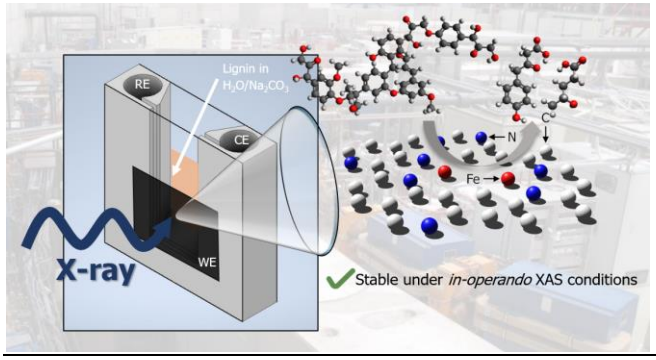

https://doi.org/10.26434/chemrxiv-2025-jnt4c **ORCID:** https://orcid.org/0000-0002-0130-8029 Content not peer-reviewed by ChemRxiv. **License:** CC BY-NC-ND 4.0